

The X-ray Emitting Components towards $\ell = 111^\circ$: The Local Hot Bubble and Beyond

Source of Acquisition
NASA Goddard Space Flight Center

K. D. Kuntz¹

*The Henry A. Rowland Department of Physics and Astronomy, The Johns Hopkins University, 3500 Charles Street,
Baltimore MD, 21218*

S. L. Snowden

Exploration of the Universe Division Goddard Space Flight Center Greenbelt MD, 20771

ABSTRACT

We have obtained an *XMM-Newton* spectrum of the diffuse X-ray emission towards $(\ell, b) = (111.14, 1.11)$, a line of sight with a relatively simple distribution of absorbing clouds; $> 9 \times 10^{19} \text{ cm}^{-2}$ at $R > 170 \text{ pc}$, a $6 \times 10^{21} \text{ cm}^{-2}$ molecular cloud at 2.5-3.3 kpc, and a total column of $1.2 \times 10^{22} \text{ cm}^{-2}$. We find that the analysis of the *XMM-Newton* spectrum in conjunction with the *RASS* spectral energy distribution for the same direction requires three thermal components to be well fit: a “standard” Local Hot Bubble component with $kT = 0.089$, a component beyond the molecular cloud with $kT = 0.59$, and a component before the molecular cloud with $kT = 0.21$. The strength of the O VII 0.56 keV line from the Local Hot Bubble, $2.1 \pm 0.7 \text{ photons cm}^{-2} \text{ s}^{-1} \text{ sr}^{-1}$, is consistent with other recent measures. The 0.21 keV component has an emission measure of $0.0022 \pm 0.0006 \text{ cm}^{-6} \text{ pc}$ and is not localized save as diffuse emission within the Galactic plane; it is the best candidate for a pervasive hot medium. The spatial separation of the $\sim 0.2 \text{ keV}$ component from the $\sim 0.6 \text{ keV}$ component suggests that the spectral decompositions of the emission from late-type spiral disks found in the literature do represent real temperature components rather than reflecting more complex temperature distributions.

Subject headings: X-rays: diffuse

1. Motivation

The original motivation for obtaining the data discussed in this paper was to constrain the X-ray spectrum of the Local Hot Bubble (LHB). The LHB is an irregular region containing the sun that is characterized by the existence of X-ray emitting gas and a deficit of neutral gas. The LHB was first discovered through the large-scale anticorrelation of $\frac{1}{4} \text{ keV}$ X-ray emission (mapped by sounding rockets) and the total column density of neutral gas (Tanaka & Bleeker 1977). The shape of the LHB was determined using the small-scale anticorrelation of $\frac{1}{4} \text{ keV}$ X-ray emission (mapped by *ROSAT* in the *RASS*) and the total column density (Snowden et al. 1990, 1998, 2000). That the region containing the X-ray emission is remarkably free of absorbing neutral material is demonstrated by three observations: the constancy of the B/Be band ratio (Juda et al. 1991), the lack of FUV absorption to a sample of nearby white dwarfs (Hutchinson et al. 1998), and the lack of local Na I absorption in stellar spectra (Sfeir et al. 1999). This last study showed that region surrounding the sun has a low density of neutral material which abruptly increases at distances of $\sim 100 \text{ pc}$ from the sun. Because the hot gas in the LHB may not completely fill the region deficient in neutral material, there

is no causal link between the X-ray emitting gas in the LHB and the deficit of local neutral material; we refer to the local low density region as the Local Cavity in order to differentiate it from the LHB.

ROSAT provided six band photometry of the emission from the LHB. Assuming collisional ionization equilibrium (CIE) and near solar abundances, the R2/R1 band ratio implies $kT \sim 0.1$ (Snowden et al. 1998; Kuntz & Snowden 2000). Given this temperature and the size scaling determined from MBM12, one can derive a crossing time of a few million years. It is thus surprising that there is a temperature gradient of $\Delta kT = 0.026$ across the LHB; the side of the LHB towards $\ell \sim 169^\circ$ being hotter than the other side (Snowden et al. 1990, 2000). As the overall Galactic emission is hotter towards the Galactic Center than the Galactic Anti-Center, the LHB gradient might, in fact, be due to some systematic problem in the separation of the local and distant emission: an inappropriate model of the spectral shape of the distant emission, or systematic errors in the column density. However, the gradient in Snowden et al. (2000) was measured at $|b| > 10^\circ$, outside of the region effected by the extended Galactic Ridge, and is not restricted to the region covered by the Loop I superbubble. Therefore the dipole is not likely due to the background emission. As the flow direction of the local ISM is towards $(\ell, b) = (183.3, -15.86)$ it is possible that the dipole is due to the interaction of the local ISM with the heliopause.

¹Mailing address: Exploration of the Universe Division, Code 662, NASA/GSFC, Greenbelt, MD 20771

The Diffuse X-ray Spectrometer (DXS) observed three regions of the LHB at high spectral resolution in the 0.148-0.284 keV band (Sanders et al. 2001). Because the count rate from the LHB is low, the spectra from these regions, covering a total of ~ 0.26 steradians from $\ell = 160^\circ$ to $\ell = 297^\circ$, were combined. The spectrum was not well fit by either CIE or non-CIE models, but $kT = 0.118$ eV with strongly depleted Mg, Fe, and Si provided the best fit. There are a number of possible reasons for the poor fit. As was pointed out by Sanders et al. (2001), the atomic data used by the models was problematic, a situation since alleviated but not completely resolved. The fitted spectrum was averaged over several regions and, although the individual spectra were statistically the same, they sample regions with different *ROSAT* temperatures. The analysis of the *DXS* data assumed a column density of 10^{21} cm $^{-2}$ immediately exterior to the LHB, while that column density is actually $\sim 10^{20}$ cm $^{-2}$ and slowly rises at greater distances (Sfeir et al. 1999). The column density of 10^{21} cm $^{-2}$ is not reached in most directions at distances < 200 pc. This difference in column density corresponds to a factor of ~ 8 difference in the transmission of 0.3 keV photons. Therefore, the LHB emission studied by DXS may be contaminated by emission from other nearby regions containing hot plasma. Although there are no distinct/discreet emission regions visible in the *RASS* within the *DXS* FOV, there clearly is emission from beyond the LHB, a point to which we shall return.

The Cosmic Hot Interstellar Plasma Spectrometer (*CHIPS*) mission attempted to measure the FUV emission from the LHB. A 0.1 keV plasma in CIE should produce Fe VIII-Fe XII lines in the 0.046-0.138 keV (90-265 Å) band. The *CHIPS* mission observed a large number of lines of sight over the entire sky for a cumulative 13.2 Ms of exposure and placed a stringent upper limit of 6 photons cm $^{-2}$ s $^{-1}$ sr $^{-1}$ on the Fe IX line at 0.072 keV (171.1 Å) which corresponds to an emission measure of 4×10^{-4} cm $^{-6}$ pc at $kT \sim 0.086$, assuming APEC/CHIANTI models and data (Hurwitz et al. 2004). The authors point out that this is 0.2 to 0.07 of that found for the soft X-ray emission by Snowden et al. (1998) using the 1991 Raymond & Smith models and solar abundances. The discrepancy becomes greater with use of more modern models and abundances. The Snowden et al. (1998) value for the soft X-ray emission (R12 band) was $2.5\text{--}8.4 \times 10^{-4}$ counts s $^{-1}$ arcmin $^{-2}$, with a R2/R1 band ratio of 1.12 ± 0.1 . Using the APEC models and Wilms et al. (2000) abundances, these values correspond to $kT = 0.0965$ keV and emission measures of 0.0062-0.0205 cm $^{-6}$ pc, factors of 150-500 greater than that observed in the FUV. Thus, if the plasma is in CIE the Fe must be extraordinarily strongly depleted to be consistent with previous soft X-ray observations of the LHB. Bellm & Vaillancourt (2005), using only the Raymond & Smith models found that a joint reanalysis of the Wisconsin rocket data and the *RASS* was marginally consistent with the *CHIPS* result.

The *CHIPS* results and the *DXS* results suggest that non-CIE models might be more appropriate. Breitschwerdt & Schmutzler (1999) modelled the LHB as

a hot plasma that has adiabatically expanded into the Local Cavity. As the gas expanded, it cooled faster than it could recombine, and the ionization temperature of the resulting plasma will depend upon the lines measured, and that temperature is much higher than the kinetic temperature. The original Breitschwerdt & Schmutzler (1999) model produced too much emission in the *ROSAT* $\frac{3}{4}$ keV (R45) band. Shelton (2002) and Smith et al. (2005) pointed out that an overionized or recombining plasma model of this sort can match the O VIII and O VII line strengths, but strongly overproduces the O VI line emission. Underionized models where the kinetic temperature is higher than the ionization temperature (i.e., the situation in shocks) are not conclusively ruled out Henley et al. (2006) but a suitable heating source has not yet been identified.

It should also be noted that the pressure of the LHB derived from the *RASS* ($P/k \sim 16000$ using CIE models, either Raymond & Smith (1977) models and Anders & Grevesse (1989) abundances or $P/k \sim 25000$ using APEC models with Wilms et al. (2000) abundances) is substantially greater than the pressure measured for diffuse neutral clouds within the LHB ($1000 < P/k < 10000$ as measured by C I absorption by Jenkins 2002). This inconsistency, the inconsistency of the X-ray results with FUV spectra (first noted with EUV (Valerga & Slavin 1998), then with *CHIPS*), and the lack of local O VI absorption (Oegerle et al. 2005), have led to the suggestion that there is no “Hot” in the Local Hot Bubble (first Cox (1998), then others). Rather than the X-ray emission being due to a hot plasma, it has been ascribed to emission from charge exchange reactions between the ionized solar wind and the neutral ISM flowing through the solar system (solar wind charge exchange or SWCX). Lallement (2004) has modeled the contribution of SWCX to the $\frac{1}{4}$ keV band of the *RASS*; the distribution of the SWCX contribution is assymetric and does not match the distribution of emission attributed to the LHB. Adjusting the scale factor of the SWCX (some combination of cross-sections and solar wind strength) to obtain the maximum possible SWCX contribution but still ensuring that the SWCX emission does not overproduce the X-ray emission attributed to the LHB in any direction, Lallement (2004) found that although the SWCX could account for all of the putative LHB emission in many directions, particularly in the Galactic plane, much of the LHB emission remains. Further the derived shape of the LHB after the limited SWCX removal is more similar to that of the Local Cavity. Simultaneously, the pressure derived from the X-ray emission drops by factors of a few.

The Lallement (2004) analysis implies that the emission previously ascribed to the LHB by the anti-correlation studies is due to both SWCX and the LHB; the observed X-ray emission observed is

$$SWCX_{min} + SWCX(t) + LHB$$

where $SWCX_{min}$ is due to some base level of solar activity, and $SWCX(t)$ is a time (and observation direction) dependent component due to the strength and geometry of the solar wind at the time of observation. The $SWCX(t)$ appropriate for the Wisconsin survey

(McCammon et al. 1983), should be different from that for the *RASS*; the uncorrected surveys should differ by $\Delta SWCX(t)$. However, the two surveys are statistically similar, suggesting that their different methods of removing $SWCX(t)$ were successful. The strength of $SWCX_{min}$ remains an open question. Snowden et al. (2004), Wargelin et al. (2004), and Kuntz & Snowden (2006) have measured spectra of the $SWCX$ in the $\frac{3}{4}$ keV band when $SWCX \gg SWCX_{min}$, but the shape of the $SWCX_{min}$ spectrum is still poorly understood.

The LHB is primarily a $\frac{1}{4}$ keV band phenomenon mapped by *ROSAT*; the ratio of the energy (photons) emitted in 0.44-1.21 keV to that in 0.111-0.284 keV is ~ 0.25 (~ 0.075). The bulk of the emission lies below the band accessible to *Chandra* and *XMM-Newton*, but some of the most important lines (O VII and O VIII) lie within the range of the current instruments/observatories. The 0.35-1.0 energy band is not nearly so sensitive to absorption as the $\frac{1}{4}$ keV band; $\tau = 1$ occurs at 10^{21} cm^{-2} rather than at 10^{20} cm^{-2} . Thus isolating the emission due to the LHB from emission at greater distances is far more difficult, particularly as the nature, amount, and disposition of the more distant emission is generally unknown.

In the face of these rather formidable challenges (measuring the spectrum in only a minor fraction of the bandpass, the difficulties of isolating the LHB from more distant emission whose characteristics are even more poorly understood, and the as yet unknown contribution by $SWCX$) we made an ambitious proposal to study the LHB with *XMM-Newton*. We proposed to observe a series of deep $\frac{3}{4}$ keV band shadows in the Galactic plane where the non-LHB emission would be minimized in order to determine the $\frac{3}{4}$ keV band spectrum of the LHB and measure the strength of the oxygen lines. The O VII and O VIII lines are sensitive diagnostics of the ionization state of the plasma and, especially when combined with the O VI lines. By measuring the line strengths in the plane over a large swath of the Galactic anticenter we hoped to place limits on the variation in the temperature and ionization structure of the LHB emission and explain the source of the R2/R1 dipole. Thus far, we have obtained only a single useful observation, which is in the direction of $\ell = 111^\circ$. However, this single spectrum demonstrates that the LHB emission can be well separated from the more distant emission, and suggests that further observations will be extremely fruitful both for studies of the LHB and for studies of the emission from beyond the LHB.

In this paper, §2 describes the data and the extraction of spectra and instrumental backgrounds, §3 describes the spectral analysis, and §4 contextualizes our results. Much of the discussion concerns the emission external to the LHB, an important but generally overlooked portion of the ISM.

2. Data

2.1. Pointing Criteria and LOS Geometry

In order to obtain the spectrum of the LHB that has the least contamination by external emission, we

chose regions with strong shadows in the *ROSAT* $\frac{3}{4}$ keV band. Most of these strong $\frac{3}{4}$ keV shadows are associated with molecular clouds, many of which have known distances. We avoided the region $-45^\circ < \ell < 45^\circ$ in order to avoid emission due to the Galactic Ridge which, although it only dominates at higher energies, could produce significant line emission below 1 keV. We chose regions where both the $\frac{1}{4}$ keV and the $\frac{3}{4}$ keV emission in the *RASS* showed no discernable emission features; this condition minimizes the non-LHB contribution, ensures that the non-LHB contribution is not due to individual SNR, and suggests that any non-LHB contribution will be representative of the typical diffuse X-ray emission in the outer Galaxy. Of our accepted targets, we obtained useful data of only one: *XMM-Newton* Obsid 0203130201, $(\ell, b) = (111.14, 1.11)$.

In the target direction the Local Cavity extends to ~ 170 pc (Sfeir et al. 1999) beyond which there is a column density of at least $9 \times 10^{19} \text{ cm}^{-2}$ (a Na D2 equivalent width of 50 mÅ). This column density is a lower limit as the total column should increase with distance. This “wall” of absorption allows 23% transmission of the more distant $\frac{1}{4}$ keV emission, blocking a significant fraction of that emission. At 2.2-3.5 kpc there is a molecular cloud (Blitz et al. 1982; Ungerechts et al. 2000), which is part of the Perseus arm. Our pointing is not on the CO peak due to the need to avoid bright optical/X-ray point sources. The $N(\text{H}_2)$ in the direction of our pointing is $3.5 \times 10^{21} \text{ cm}^{-2}$ (Ungerechts et al. 2000), meaning that $N(\text{H}) > 6 \times 10^{21} \text{ cm}^{-2}$, providing a strong but distant “backstop”; X-rays from beyond the cloud with $E < 0.6$ are effectively blocked.

The total column density in this direction (including the molecular cloud) is $\sim 1.1 \times 10^{22} \text{ cm}^{-2}$ which effectively blocks emission from the Galactic halo and extragalactic sources at energies below 1 keV. We define the emission beyond the molecular cloud to be the “distant” component and emission between the Local Cavity and the cloud to be the “intermediate” component. The intermediate component is absorbed by the wall of absorption immediately external to the LHB. This absorption is almost complete below ~ 0.4 keV, but the intermediate distance component could contribute to the O VII emission at 0.56 keV and the O VIII emission at 0.65 keV.

2.2. Reduction

Since our current understanding of the particle background of the *XMM-Newton* pn camera is relatively poor, and the characterization of the background of the *XMM-Newton* MOS cameras is fairly well refined, we have restricted our analysis to the data obtained by the two MOS cameras. The data reduction follows the “standard” method described in Kuntz & Snowden (2006) and Snowden & Kuntz (2006). We constructed the light curve in the 2.5-8.5 keV band for the entire FOV. We fitted a Gaussian to a histogram of the count rates, and set the “quiescent level” to the mean of that Gaussian. We removed from further analysis all time periods during which the count rate was $> 3\sigma$ above the quiescent level; the higher count rate in those time periods is due to either strong soft proton contamination

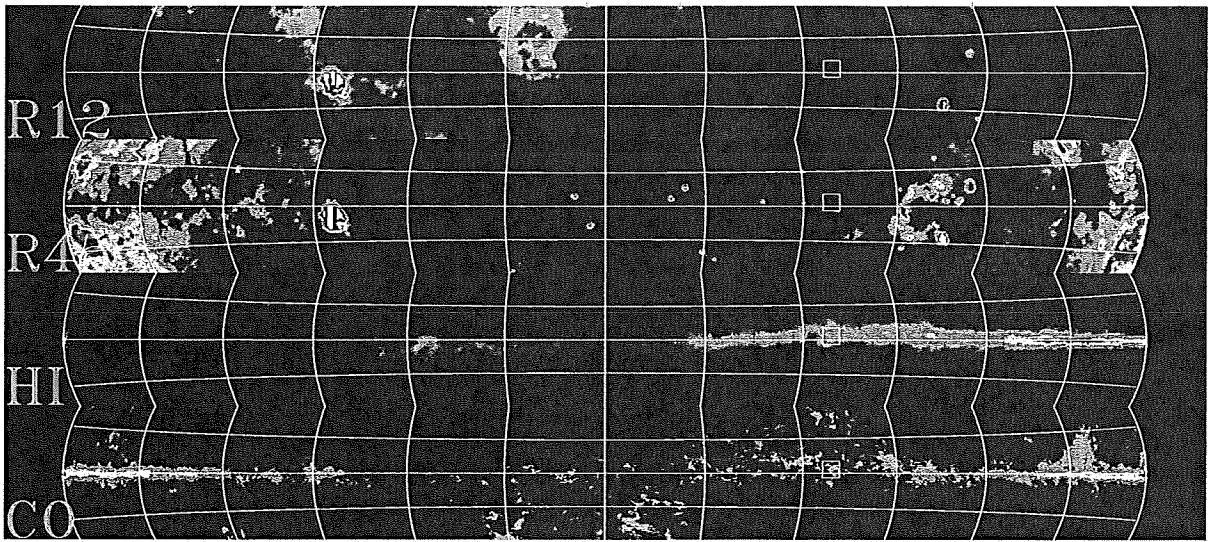


Fig. 1.— Location of the observation with respect to the X-ray sky and the absorbing column density. **Top:** The R12 band flux from the *RASS*. The color scale runs linearly from 0 to 2.5×10^{-3} counts $\text{s}^{-1} \text{ arcmin}^{-2}$ and pixels above that value were clipped. The Aitoff projection is centered on $\ell = 180^\circ$, the longitude is marked every 30° and increases to the left, the latitude is marked every 10° . The box marks the location of the observation. **Upper Middle:** The R45 band flux from the *RASS*. The color scale runs linearly from 0 to 7.5×10^{-4} counts $\text{s}^{-1} \text{ arcmin}^{-2}$. **Lower Middle:** The HI from the Leiden-Dwingeloo Survey (Hartmann & Burton 1997). The color scale runs linearly from 0 to 10^{22} cm^{-2} . **Bottom:** The CO map from Dame et al. (2001). The color scale runs logarithmically from 0 to 1474 in W_{CO} , or a hydrogen nucleon density of $5.3 \times 10^{23} \text{ cm}^{-2}$.

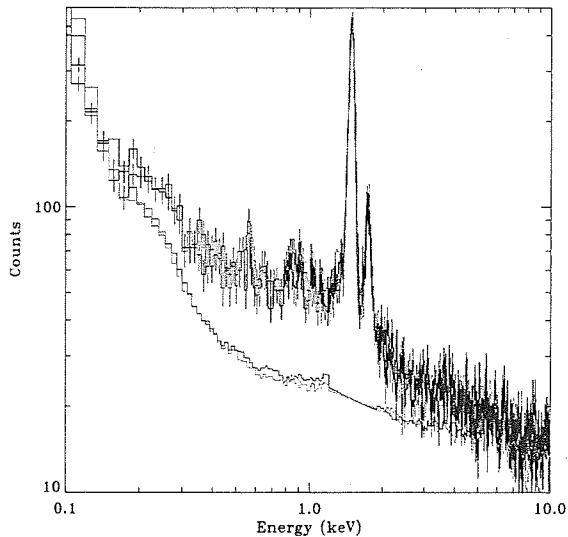


Fig. 2.— The raw spectra for MOS1 (black) and MOS2 (blue), and the constructed quiescent particle background spectra for MOS1 (green) and MOS2 (red). The spectra were not used below 0.3 keV, nor above 8 keV. The Al and Si lines at 1.48 and 1.75 keV were not included in the quiescent background spectra but were fit during analysis. The contribution from soft proton flares is also not included in these background spectra.

or an enhanced particle background. Of the original 22.5 ks of exposure, cleaning left 21.5 ks.

Source detection was performed in both the 0.3-2.0 keV and 2.0-10.0 keV bands. Sources with a maximum likelihood detection value greater than 40 in either band (corresponding to $\sim 10^{-13} \text{ ergs cm}^{-2} \text{ s}^{-1}$) were removed. For each source to be removed we determined the 80% encircled energy radius using the model PSF for the distance of the source from the optical axis. Source exclusion radii were typically 24-29 arcseconds. The few remaining faint point sources are likely to be background AGN with a power-law spectrum which is unlikely to confuse our analysis of thermal spectra. The amount of emission due to unresolved stars is a more difficult issue (Kuntz & Snowden 2001). The spectrum of the diffuse emission was extracted from a region with a radius of $14'$ approximately centered on the optical axis.

We constructed the spectrum of the “quiescent particle background” from the “unexposed pixel” data and filter-wheel-closed data. The background spectrum is interpolated over the 1.2-1.9 keV interval before being subtracted from the observed spectrum; the Al and Si instrumental lines at ~ 1.48 and ~ 1.74 keV were left in the observed spectrum and were fitted during analysis. The strength of the residual soft proton flares is not known *a priori*, but the shape is reasonably well modeled by a broken power law with a break energy of 3.2 keV, where the spectrum is convolved with the redistribution matrix but not scaled by the response function. The contribution of the residual soft proton flares is fitted during the analysis.

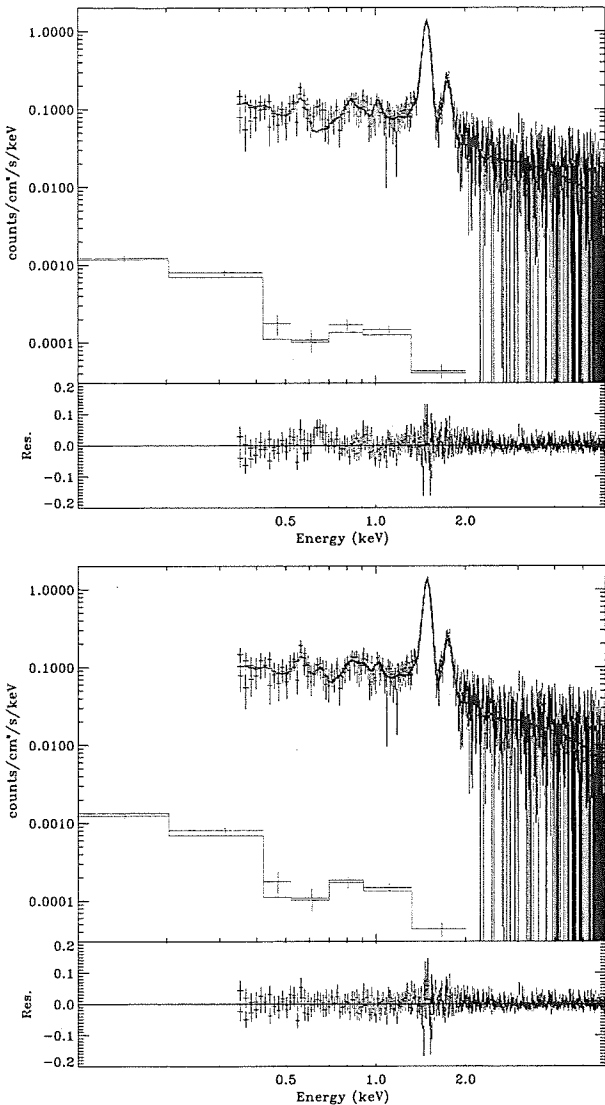


Fig. 3.— **Top:** Two-component simultaneous model fit to both MOS spectra and the *RASS* spectral energy distribution. **Bottom:** Three-component model fit to the same spectra.

3. Spectral Analysis

Since the bulk of the LHB emission is at energies below the *XMM-Newton* bandpass, we must constrain the fit so that it is consistent with other measures of the LHB at the lower energies. We constrain the fit by simultaneously fitting the *RASS* data from a half degree radius circle centered on $(\ell, b) = (111.14, 1.11)$ with the two MOS spectra. The *RASS* data was extracted using the X-ray background tool at the HEASARC² and consists of a seven band spectral energy distribution (bands R1 through R7) with statistical uncertainties. The non-statistical uncertainties due to the removal of Long Term Enhancements depend upon the location in the survey; the $\ell = 111^\circ$ LOS is located in a region where the non-statistical uncertainties are low.

²<http://heasarc.gsfc.nasa.gov/cgi-bin/Tools/xraybg/xraybg.pl>

The two MOS spectra were fitted in XSPEC 11.3.2 with the following function

$$k(N_L A_L(T, z) + e^{\tau_{local}} N_I A_I(T, z) + e^{\tau_{cloud}} N_D A_D(T, z) + e^{\tau_{total}} N_\Gamma E^{-\Gamma}) + Al + Si + SPC$$

where k is the size of the FOV in arcminutes. The $A(T, z)$ are thermal components representing the emission from the LHB (L), emission in front of the molecular cloud (the intermediate component, I), and emission from beyond the molecular cloud (the distant component, D). The N are the model normalizations. We used the APEC models (Smith et al. 2001) where the abundances, z , are on the Wilms et al. (2000) scale. The absorption of the intermediate distance component is $> 9 \times 10^{19} \text{ cm}^{-2}$ and is likely higher; it was allowed to float above its minimum value. The absorption of the distant component was set to no smaller than $6 \times 10^{21} \text{ cm}^{-2}$. The $e^{\tau_{total}} N_\Gamma E^{-\Gamma}$ represents the contribution by the unresolved AGN absorbed by the entire Galactic column. We set $\Gamma = 1.46$ (Chen et al. 1997) and $N = 10.5 \text{ keV cm}^{-2} \text{ s}^{-1} \text{ sr}^{-1} \text{ keV}^{-1}$. Allowing the normalization to float did not produce significant changes. The *Al* and *Si* are Gaussians representing the instrumental lines. For the initial fits the line centers of the *Al* and *Si* lines were fixed, the line widths were set to zero, and the amplitudes for the two MOS spectra were made to agree. The *SPC*, the soft proton contamination, was modeled by a broken power law with a break energy of 3.2 keV (Kuntz & Snowden 2006). For the initial fits, the amplitude of this component was set to zero. As the fits converged, the amplitude and the indices were allowed to vary, but the indices for the two MOS spectra were forced to be equal. The *RASS* “spectrum” was fitted with the same function but without the instrumental lines or soft proton component.

This is a rather complicated functional form to be fit to a single spectrum, so we began by fitting a simpler model. We know (or at least expect) that there is emission due to the LHB. We also know that there is emission from beyond the molecular cloud since we observed a shadow there in the *RASS*. We began by fitting without the intermediate distance component, by fixing the effective Mg, Si, Fe, and Ni abundances for the LHB to the values found by Sanders et al. (2001) setting all the other LHB abundances to solar, and allowing the abundance of Mg, Si, Fe, and Ni of the distant component to float.

The result of fitting this two component (local+distant) model can be seen in Figure 3. The fit parameters are listed in Table 1. Although the reduced χ^2 is good, the fit is poor; there are strong residuals at O VIII 0.65 keV and at O VII 0.56 keV. The O VIII line cannot be produced by the distant component; the O VIII line is too heavily absorbed to be consistent with the flux at higher energies. The O VIII line cannot be produced by the LHB; no model producing a significant O VIII emission can produce the correct R2/R1 ratio and the relative strengths of the R12 band emission and O VII 0.56 keV emission. Granted, we are using CIE models here, and CIE models need not be applicable, but the observational result of Smith et al. (2006) where no

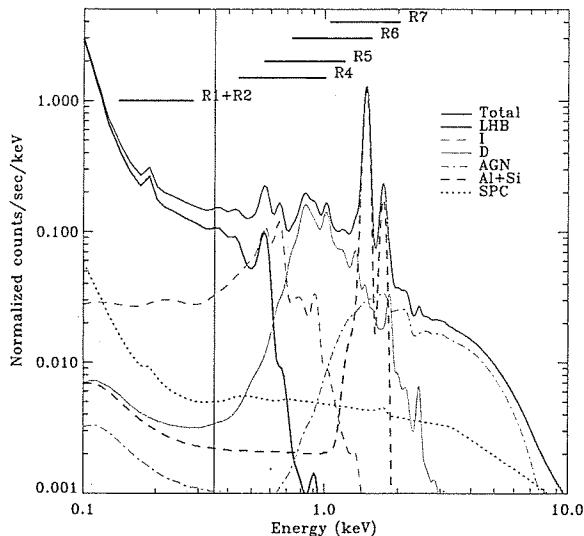


Fig. 4.— The three-component model decomposed into its constituent parts.

O VIII line was seen towards the nearby dense molecular cloud MBM 12 also argues strongly that the O VIII is not produced by the LHB.

Having ruled out both the LHB and distant components as the source of the O VIII line, one must introduce the intermediate distance component. We have assumed that the intermediate distance component has the same abundances as the LHB. The fit is again shown in Figure 3 and the fit parameters are listed in Table 1. The O VIII line is properly fit though a residual remains at the O VII line. An additional Gaussian was added with $E = 0.55$ keV, but this component did not have a significant flux even when all the other components were allowed to float; the residual appears to be slightly narrower than the line spread function. A decomposition of the model appears in Figure 4.

To understand the extent to which the three-parameter fit is better than the two-parameter fit, we used the two-parameter model and the measured backgrounds to create one thousand simulated spectra, each of which was fit with both the two- and three-parameter models. For the fit to the data, $\Delta\chi^2 \equiv \chi^2_{2comp} - \chi^2_{3comp} = 24.5$. For the Monte-Carlo simulations, less than half a percent of the trials had $\Delta\chi^2 > 24.5$. The observed $\Delta\chi^2$ is statistically unlikely if the two-component model were an adequate representation of reality. Therefore, a three-component model is a significantly better representation of the data than the two-component model.

From the fit uncertainties, the results appear robust. The uncertainties in the LHB parameters are $\sim 10\%$, the uncertainties in the intermediate component parameters are 20-25%, and the uncertainties in the distant component parameters are 10% in kT , 35% in normalization and 50% in abundance. The uncertainties in the LHB parameters are certainly underestimates as they do not include the uncertainty in the abundances.

The uncertainties in the intermediate component are high because it is easy for the fit to shift flux from the intermediate component to the distant component. Interestingly, the distant component has a well constrained temperature, even if its normalization is not so well constrained.

To understand the robustness of our results, we fit the spectrum with three-parameter models where the LHB abundance of Mg, Si, Fe, and Ni was varied from 0.1 solar to solar, and the absorption immediately outside the LHB was varied from $1 \times 10^{20} \text{ cm}^{-2}$ to $1 \times 10^{21} \text{ cm}^{-2}$. The behavior of the remaining fit parameters is summarized in Figure 5. As the z_L is decreased (from solar) kT_L decreases and N_L increases. This is due to the fact that the R1 and R2 bands contain many lines from Mg, Si, Fe, and Ni, the R1 band being more strongly affected than the R2 band. Decreasing z_L increases R1/R2, requiring kT_L to decrease to compensate, and decreases R1+R2, requiring N_L to increase to compensate. However, in the temperature range allowed by the *ROSAT* values, the O VII/(R1+R2) increases with kT , but O VIII/(R1+R2) increases negligibly. Thus, the fit of the LHB component is driven by R2/R1, O VII/(R1+R2) (as modified by the intermediate component), and the absolute value of R1+R2.

Given the sensitivity of the LHB parameters to the *RASS* data, one might wonder to what extent the fit is sensitive to the uncertainties in the *RASS* spectral energy distribution. If, instead of using the (R1,R2) values, one fits with the constraint of $(R1+\sigma_{R1}, R2-\sigma_{R2})$ or $(R1-\sigma_{R1}, R2+\sigma_{R2})$ then the fit changes by an amount smaller than the 90% uncertainty.

The intermediate component supplies the O VIII line and, as a result, contributes to the O VII line as well. Therefore, kT_I is driven by the amount of O VII not produced by the LHB and thus kT_I is driven primarily by z_L . N_I is driven primarily by the absorption, $N(H)_{wall}$. If one allows $N(H)_{wall}$ to float, the best fit value is $1.6 \times 10^{21} \text{ cm}^{-2}$ where the uncertainty is much larger than the value. Although $N(H)_{wall}$ is not constrained by the X-ray data, even at its highest values, kT_I does not change significantly.

Since $z_I \equiv z_L$, the amount of emission contributed by the intermediate component to the line complexes in $0.7 < E < 1.0$ keV decreases with z_L . That emission, in turn, must be supplied by the distant component, causing kT_D to decrease, z_D to increase, and N_D to decrease. Without the $z_I \equiv z_L$ linkage, the distant component would be insensitive to the LHB parameters. Even with the $z_I \equiv z_L$ linkage, the variation of the distant component parameters with the LHB parameters is less than the statistical uncertainties; the distant component is very well constrained.

It should be noted that although we have set $z_L = 0.3$ on the strength of the DXS data, the best fits in our parameter search are obtained with $z_L = 1.0$; the R2/R1 value of the *RASS* data is more closely matched, and the overall R1+R2 strength is more closely matched. The z_L is very sensitive to the relative normalizations of the *RASS* and *XMM-Newton* data. Since the $z_L = 0.3$ was determined from high resolution data in the $\frac{1}{4}$ keV band, that value is prefer-

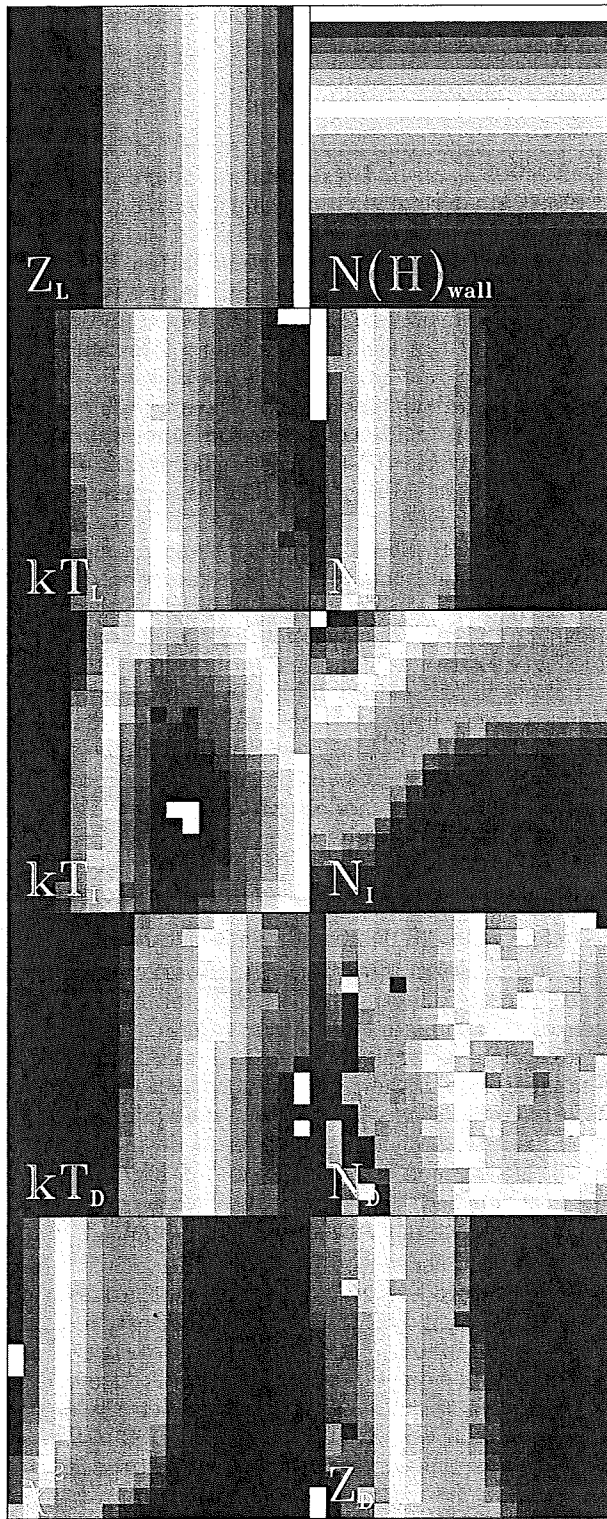


Fig. 5.— Diagrams demonstrating the response of the fit parameters to variation in z_L (top left diagram) and $N(H)_{wall}$ (top right diagram). The color scales run from black/purple at the lowest values to red/white at the highest values. The limits for each panel are: z_L : 0.1 to 1.0, $N(H)_{wall}$: 10^{20} to 10^{21} cm $^{-2}$, kT_L : 0.0808 to 0.1035 keV, N_L : 1.48×10^{-6} to 3.77×10^{-6} , kT_I : 0.2108 to 0.2611 keV, N_I : 3.95×10^{-7} to 8.84×10^{-7} , kT_D : 0.5625 to 0.7675 keV, N_D : 3.79×10^{-6} to 4.06×10^{-6} , $\Delta\chi^2$: -8.81 to 13.40 (compared to $z_L = 0.33$ and $N(H)_{wall} = 10^{20}$ cm $^{-2}$), and z_d : 0.52 to 0.77.

able to that found by our parameter search.

3.0.1. SWCX

The X-ray spectrum may be contaminated by emission due to ions in the solar wind interacting with neutral interplanetary material. The strength and spectral shape of this solar wind charge exchange (SWCX) emission is still poorly characterized; it will depend upon many interaction cross-sections, the strength and ionization structure of the solar wind, as well as the neutral density of the interplanetary material along the entire line-of-sight to the heliopause. During a particularly strong gust of the solar wind, with a special viewing geometry through the densest part of the magnetosheath, Snowden et al. (2004) detected the SWCX emission with *XMM-Newton*. However, the spectrum of the “typical” SWCX contamination, the $SWCX_{min}$ emission studied by Lallement (2004), is not known.

Our observation was taken when the spacecraft was pointed through the low-density flanks of the earth’s magnetosheath at an angle of 106° from the sun. The *ACE* data for the time of observation suggests that the solar wind was quite quiescent; the solar wind flux was steady around 1.4×10^8 cm $^{-2}$ s $^{-1}$ which is lower than 88% of solar wind measurements. The O^{+7}/O^{+6} ratio was typical of the solar wind; the O^{+8}/O^{+7} ratio was not available for the time of observation. Given the observation geometry and that the solar wind was a relatively light breeze the SWCX contamination of this observation is expected to be “typical”; the expected X-ray spectrum is thus expected to be very close to $SWCX_{min} + LHB$.

The significant SWCX contamination consists entirely of lines; the SWCX spectrum obtained by Snowden et al. (2004) consisted of C VI, O VII, O VIII, Ne IX and Mg XI. The relative strengths of these lines vary as the ionization structure of the solar wind varies. We have added this model of the SWCX to our two-component model; although the addition of the SWCX to the model did improve the fit ($\Delta\chi^2 = 12.0$ for 793 d.o.f) it did not improve the fit to the same extent as the addition of a third thermal component ($\Delta\chi^2 = 24.5$). If one allows all of the SWCX lines to vary independently, only the O VII 0.56 keV, O VIII 0.65 keV, and the Mg XI 1.34 keV lines are allowed in significant quantities. In particular, the O VIII 0.81 keV line seen by Snowden et al. (2004) is not seen in this spectrum, suggesting that O VIII 0.65 keV line cannot be explained solely through SWCX. This exercise also demonstrates that the spectrum of $SWCX_{min}$ is not like $SWCX(t)$ unless the total contribution of $SWCX_{min}$ is very small.

4. Discussion

The analysis above produces the following understanding of the $\ell = 111^\circ$ line of sight. The LHB has emission characteristic of a $kT_{LHB} = 0.089$ keV plasma, where that temperature is very sensitive to the assumed abundance of Mg, Si, Fe, and Ni, the principal strongly depleted species producing lines in the $\frac{1}{4}$ keV band. Outside of the LHB, $R > 170$ pc, there is absorption $N(H)_{wall} > 9 \times 10^{19}$, beyond which there

is emission due to a plasma with $kT_{int} = 0.241$ keV. The exact location of this emission is uncertain, but it must be closer than 2.5-3.3 kpc where there is a molecular cloud. Beyond the molecular cloud there is emission characteristic of $kT_{dis} = 0.569$. There may be cooler components beyond the molecular cloud, but their emission would be almost completely absorbed by the molecular cloud.

4.1. LHB

The model fits correspond to a O VII 0.56 keV line strength of $1.86^{+0.54}_{-0.75}$ photons $\text{cm}^{-2} \text{s}^{-1} \text{sr}^{-1}$, for an R12 band flux of 3.19×10^{-4} counts $\text{s}^{-1} \text{arcmin}^{-2}$.

The *Suzaku* measure of the O VII 0.56 keV line in the direction of the high latitude molecular cloud MBM 12, where more distant emission is almost completely blocked, is 2.3-3.5 photons $\text{cm}^{-2} \text{s}^{-1} \text{sr}^{-1}$ for an LHB R12 band flux of 3.47×10^{-4} counts $\text{s}^{-1} \text{arcmin}^{-2}$ (Smith et al. 2006; Kuntz et al. 1997), for an O VII/R12 ratio of $(5.6-8.5) \times 10^{-4}$ photon/count. Our characterization of the LHB is derived from a combination of *ROSAT* band values and (compared to *Suzaku*) poorer spectral resolution *XMM-Newton* data for a more complicated line-of-sight but it is still consistent with the *Suzaku* data; we get O VII/R12 ratio of $(6.3 \pm 2.2) \times 10^{-4}$ photon/count where both the O VII count rate and foreground R12 band rate are calculated from our model fit. We will shortly be testing the consistency of the *XMM-Newton* data directly with a *Suzaku* observation of this LOS.

Another measure of the LHB emission is provided by Henley et al. (2006) who studied the line of sight towards an absorbing filament at $(\ell, b, R) = (278.7, -45.3, 230 \text{ pc})$. Using a combination of *XMM-Newton* and *RASS* data they found $kT_{LHB} = 0.099^{+0.005}_{-0.009}$ and an O VII 0.56 keV line strength of 4.1 ± 0.6 photons $\text{cm}^{-2} \text{s}^{-1} \text{sr}^{-1}$; the O VII/R12 ratio is $(9.1 \pm 1.3) \times 10^{-4}$ photon/count, roughly consistent with the other values.

Our result, especially coupled with those of Smith et al. (2006) and Henley et al. (2006), demonstrates that the LHB does not produce measurable O VIII emission or significant R45 band flux. Given that we know the $N(\text{H})_{\text{wall}} > 9 \times 10^{19}$, and the best fit value is greater than this minimum, we are led to the conclusion that the higher temperature intermediate component truly resides outside of the local cavity. This result contrasts starkly with the results of Breitschwerdt et al. (2005) who find the LHB to be characterized by two thermal components with $kT = (0.14 \pm 0.04, 0.20 \pm 0.06)$ keV. These temperatures are based on their analysis of a line of sight towards the Bok globule Barnard 68, $(\ell, b, R) = (7.09^\circ, 1.54^\circ, 125 \text{ pc})$, a molecular cloud with a column density of $\sim 10^{23} \text{ cm}^{-2}$. This cloud lies within the Loop I superbubble. Breitschwerdt et al. (2005) argue that the emission before the cloud is not strongly contaminated by the Loop I superbubble because Fe lines due to Loop I seen off the cloud are not seen towards the cloud. This is clearly a very complicated line of sight with the cloud lying behind the working surface of an expanding super bubble and lying in front of the Galactic Ridge (a possible source of the Fe lines). The understanding of the entire line of sight towards

Barnard 68 is not yet sufficient to consider this a significant detection of the LHB.

4.1.1. SWCX

The spectrum analysed above is the spectrum of $SWCX_{min} + LHB$, and we have assumed that $SWCX_{min}$ is small. Assuming otherwise, with our current lack of understanding of $SWCX_{min}$, leads to an unmanageably large set of possibilities. If one assumes depletions equivalent to Mg, Si, Fe, and Ni abundances of 0.33, and uses the Fe IX 0.072 keV line to place an upper limit on the true amount of thermal emission from a CIE model, one finds that at $kT = 0.086$ the thermal emission can account for only 4% of the O VII or 9% of the R12 band emission. Increasing the temperature to $kt \sim 0.11$ boosts that fraction to 20% of the O VII or 11% of the R12 band emission, as the emissivity of Fe IX drops above $kT = 0.8$. The O VII line emission places a slightly tighter constraint than the R12 band emission. These values were calculated for the $\ell = 111^\circ$ line of sight, a direction that the Lallement (2004) map suggests retains a significant amount of true LHB emission. Our results indicate that a hot bubble is still compatible with the *CHIPS* constraint given some help from the SWCX. It should also be noted that $SWCX_{min}$ contribution to the O VII line also produces significant changes in the recombination models, allowing models with much lower kT and n_e than previously explores.

4.2. The Intermediate Distance Component

Snowden (2001) has pointed out that the bulk of the $\frac{1}{4}$ keV emission in the solar neighborhood is associated with discrete features; the LHB, and the Eridion bubble. The same is clearly not true at $\frac{3}{4}$ keV; with the exception of discrete sources such as SNR and the Loop I superbubble, the $\frac{3}{4}$ keV sky appears to be quite uniform, varying only a little from Galactic pole to Galactic equator. This uniformity exists despite the fact that a large fraction of the emission at high Galactic latitudes is due to unresolved AGN whose contribution at the Galactic equator should be minimal.

Figure 6 shows the $\frac{3}{4}$ keV (R45 band) sky in $90^\circ < \ell < 270^\circ$ from the *RASS* cast into Cartesian coordinates. Bright point sources, bright extended sources (such as Monogem, the Eridion Bubble), and areas of missing data have been masked out. Also removed is the region without data in the Leiden-Dwingaloo H I survey (Hartmann & Burton 1997). At this stretch one can see residual systematic scan-to-scan variation as streaks following lines of constant ecliptic longitude; otherwise the sky appears rather uniform.

Figure 6 shows the latitudinal profile for the R4-R7 bands for the $120^\circ < \ell < 230^\circ$ range, as well as the expected profile due to the extragalactic background and Galactic halo after absorption by the Galactic disk. The absorption was calculated with the H I column from the Leiden-Dwingaloo survey and the CO column from Dame et al. (2001). The top set of profiles shows the residuals (observed-model) which are clearly peaked at $b = 0^\circ$. A secondary peak at $b \sim -18^\circ$ is possibly due to scan path residuals between $\ell = 130^\circ$ and $\ell = 150^\circ$.

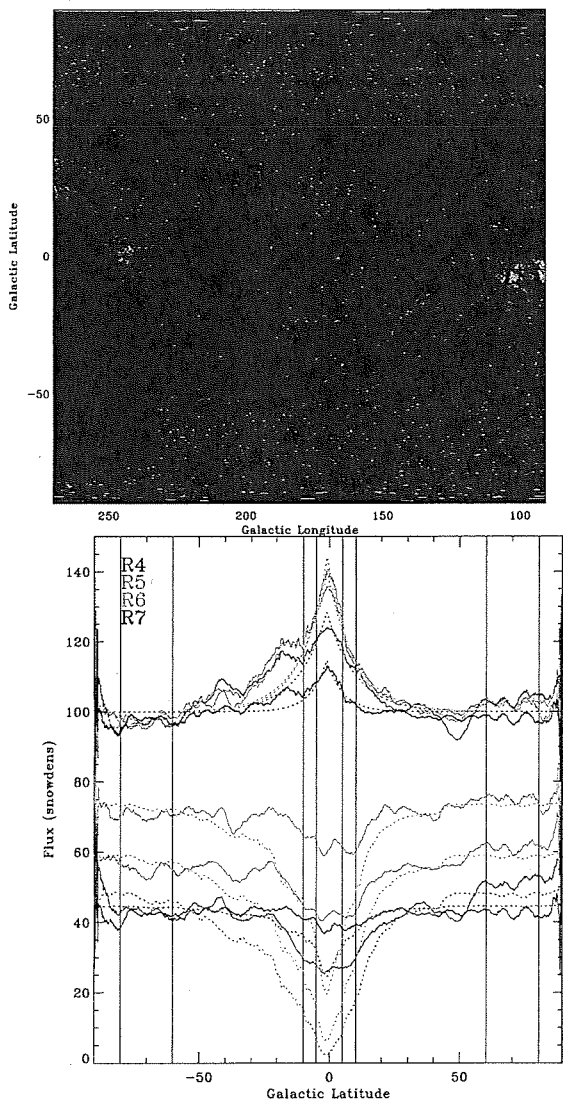


Fig. 6.— **Top:** The R45 band sky in Cartesian coordinates. The latitudes $\pm 10^\circ$, $\pm 5^\circ$ and 0° are marked. The black regions denote excised data, either due to poor background subtraction for a set of ecliptic scans, bright extended sources, or bright point sources. **Bottom:** The lower sets of solid lines are the observed band profiles. The overplotted dotted profiles are the models of the Galactic halo and extragalactic background absorbed by the Galactic disk. The upper sets of solid lines are the observed band profiles from which the model has been subtracted. The dotted overplotted profiles are an exponential model.

Fitting an exponential to the data for $b > -10^\circ$ finds scale-heights of $\sim 10^\circ$ for bands R4-R6, $\sim 6^\circ$ for band R7. This emission from the Galactic disk is composed, no doubt, of many different emission components interleaved with many different absorption components. Given this mixture and the low *RASS* count-rates, it is impossible to characterize the emission using *ROSAT* band ratios. However, given the grasp of *XMM-Newton* and its spectral resolution, studies of lines of sight such as the one we are describing here whose absorption structure is relatively simple can separate the components along lines of sight.

Studies of diffuse X-ray emission in other galaxies, show that the emission follows the spiral arms and is primarily due to star formation (Kuntz et al. 2003; Tyler et al. 2004). The $\frac{3}{4}$ keV shadows in $100^\circ < \ell < 150^\circ$ (visible in Figure 1) are due to molecular clouds in the Perseus arm. The distant component is beyond those clouds and is probably dominated by X-ray emission due to the star-formation in the Perseus arm. The intermediate component is likely not in the inter-arm region but is either on the front side of the Perseus arm or in the local arm. Individual star-forming regions at the distance of the Perseus arm (2.5-3.3 kpc) should be distinguishable as discrete features with sizes comparable to that of the cloud shadows. As there a number of star-forming regions near this line of sight within our local arm (see, for example Becker & Fenkart 1970), it seems more likely that the intermediate component is due to local arm star-formation. Since there are a number of cloud shadows due to the Perseus arm along the plane, similar studies of those shadows would allow one to assess the uniformity of the strength and temperature of the intermediate component which would, in turn indicate to which arm the emission belongs.

If we assume that the intermediate distance component is associated with the local arm and thus has $0.2 \lesssim R \lesssim 1$ kpc, we find $n_e \sim 0.0016 \text{ cm}^{-3}$ and $P/k > 10000 \text{ K cm}^{-3}$ assuming a filling factor of unity. The 0.1-10.0 keV surface brightness is $6.3 \times 10^{-16} \text{ ergs cm}^{-2} \text{ s}^{-1} \text{ arcmin}^{-2}$. If one assumes that the vertical extent of the emission is roughly equal to the observed pathlength through the plasma then the intermediate distance component would appear to 5-10 times weaker than the typical emission from the inner disk of the face-on galaxy M101.

4.3. On Other Spiral Disks

The spectra of the diffuse emission from late-type spiral disks can generally be modelled by two thermal components with temperatures of $kT \sim (0.2, 0.6)$. The spectra used in these studies typically sum over large portions of the galactic disk in order to obtain sufficient counts to allow spectral fitting. Therefore the consistency of the results may be due to averaging the spectrum across the disk. Kuntz et al. (2003) showed that for M101 (which may not be representative) the ratio of the emission measures of the two thermal components was statistically constant across the disk, so averaging is probably not responsible.

One can show (Kuntz 2006) that most continuous distributions of emission measures with $0.1 < kT < 0.8$,

when modeled at *Chandra* spectral resolution, produce two components with $kT \sim (0.2, 0.6)$, independent of the shape of the distribution of emission measures. Thus, the consistency of the galactic results may be due to a lack of spectral resolution. These are also the two temperatures that characterize the diffuse X-ray emission from Galactic star forming regions such as the Rosette and Omega nebulae (Townsley et al. 2003).

What the current study shows is that $kT \sim (0.2, 0.6)$ probably is representative of the true gas temperatures. The intermediate distance component is constrained to lie between ~ 0.2 kpc and 2-3 kpc. If the emission is distributed throughout the allowable portion of the line of sight, then one could imagine that there is a distribution of temperatures since the crossing time is tens of millions of years(?). Even in this case the temperature distribution must be rather narrowly peaked around 0.2 keV; the intermediate distance component is not intermixed with hotter (0.6 keV) gas. Since the distant component is strongly absorbed, it is impossible to know whether it is intermixed with 0.2 keV gas. For both components it is reasonably clear that the fitted temperature represents, at worst, a narrow range of temperatures, rather than the effects of spectral resolution. Thus it seems more probable that the temperatures observed for the diffuse emission in other galaxies actually represent individual thermal components.

This research was supported by grants from the *XMM-Newton* Guest Observer Facility at NASA.

REFERENCES

- Anders, E., & Grevesse, N. 1989, *Geochim. Cosmochim. Acta*, 53, 197
- Becker, W., & Fenkart, R. 1970, in *The Spiral Structure of the Galaxy*, ed. W. Becker & G. Contopoulos, 205
- Bellm, E. C., & Vaillancourt, J. E. 2005, *ApJ*, 622, 959
- Blitz, L., Fich, M., & Stark, A. A. 1982, *ApJS*, 49, 183
- Breitschwerdt, D., de Avillez, M., & Freyberg, M. 2005, in *The Young Local Universe*, ed. T. Montmerle, A. Chalabaev, & J. T. T. Van, astro-ph/0501586
- Breitschwerdt, D., & Schmutzler, T. 1999, *A&A*, 347, 650
- Chen, L.-W., Fabian, A. C., & Gendreau, K. C. 1997, *MNRAS*, 285, 449
- Cox, D. P. 1998, in *The Local Bubble*, ed. D. Breitschwerdt & M. Freyberg, 121
- Dame, T. M., Hartmann, D., & Thaddeus, P. 2001, *ApJ*, 547, 792
- Hartmann, D., & Burton, W. B. 1997, *Atlas of Galactic Neutral Hydrogen* (Cambridge University)
- Henley, D. B., Shelton, R. L., & Kuntz, K. D. 2006, *ApJ*, submitted
- Hurwitz, M., Sasseen, T. P., & Sirk, M. M. 2004, *ApJ*, 623, 911
- Hutchinson, I. B., Warwick, R. S., & Willingale, R. 1998, in *The Local Bubble*, ed. D. Breitschwerdt & M. Freyberg, 283
- Jenkins, E. B. 2002, *ApJ*, 580, 938
- Juda, M., Bloch, J. J., Edwards, B. C., McCammon, D., Sanders, W. T., Snowden, S. L., & Zhang, J. 1991, *ApJ*, 367, 182
- Kuntz, K. D. 2006, *BAAS*, 208, 4922, and forthcoming work
- Kuntz, K. D., & Snowden, S. L. 2000, *ApJ*, 543, 195
- Kuntz, K. D., & Snowden, S. L. 2001, *ApJ*, 554, 684
- Kuntz, K. D., & Snowden, S. L. 2006, *ApJ*, submitted
- Kuntz, K. D., Snowden, S. L., Pence, W., & Mukai, K. 2003, *ApJ*, 588, 264
- Kuntz, K. D., Snowden, S. L., & Verter, F. 1997, *ApJ*, 484, 245
- Lallement, R. 2004, *A&A*, 418, 143
- McCammon, D., Burrows, D. N., Sanders, W. T., & Kraushaar, W. L. 1983, *ApJ*, 269, 107
- Oegerle, W. R., Jenkins, E. B., Shelton, R. L., Bowen, D. V., & Chayer, P. 2005, *ApJ*, 622, 377
- Raymond, J. C., & Smith, B. W. 1977, *ApJS*, 35
- Sanders, W. T., Edgar, R. J., Kraushaar, W. L., McCammon, D., & Morgenthaler, J. P. 2001, *ApJ*, 554, 694
- Sfeir, D., Lallement, R., Crifo, F., & Welsh, B. Y. 1999, *A&A*, 346, 785
- Shelton, R. 2002, *ApJ*, 569, 758
- Smith, R. K., et al. 2006, *PASJ*, submitted
- Smith, R. K., Brickhouse, N. S., Liedahl, D. A., & Raymond, J. C. 2001, *ApJ*, 556, L91
- Smith, R. K., Edgar, R. J., Plucinsky, P. P., Wargelin, B. J., Freeman, P. E., & Biller, B. A. 2005, *ApJ*, 623, 225
- Snowden, S. L. 2001, *The Century of Space Science*, ed. J. Bleeker, J. Geiss, & M. Huber (Kluwer), Ch. The ISM, The Hot Part
- Snowden, S. L., Collier, M., & Kuntz, K. D. 2004, *ApJ*, 610, 1182
- Snowden, S. L., Cox, D. P., McCammon, D., & Sanders, W. T. 1990, *ApJ*, 354, 211
- Snowden, S. L., Egger, R., Finkbeiner, D., Freyberg, M. J., & Plucinsky, P. P. 1998, *ApJ*, 493, 715
- Snowden, S. L., Freyberg, M. J., Kuntz, K. D., & Sanders, W. T. 2000, *ApJS*, 128, 171

TABLE 1
FIT PARAMETERS

Parameter	2 Comp.		3 Comp.		Units
	Value	σ^a	Value	σ^a	
kT_{LHB}	0.0988	+0.0049 -0.0053	0.0894	+0.0072 -0.0081	keV
N_{LHB}	0.0128	+0.0015 -0.0014	0.0126	+0.0014 -0.0013	cm ⁻⁶ pc
kT_{int}	0.2414	+0.065 -0.043	keV
N_{int}	0.0022	+0.0006 -0.0006	cm ⁻⁶ pc
kT_{dis}	0.312	+0.051 -0.018	0.5699	+0.039 -0.044	keV
z_{dis}	0.65	+0.28 -0.12	0.6787	+0.34 -0.26	
N_{dis}	0.0452	+0.0060 -0.0011	0.0191	+0.0065 -0.0042	cm ⁻⁶ pc
χ^2	750		725		
d.o.f.	796		794		

^a90% uncertainty interval

- Snowden, S. L., & Kuntz, K. D. 2006, ApJ, in preparation
- Snowden, S. L., Schmitt, J. H. M. M., & Edwards, B. C. 1990, ApJ, 364, 118
- Tanaka, Y., & Bleeker, J. A. M. 1977, Space Sci. Rev., 20, 815
- Townsley, L. K., Feigelson, E. D., Montmerle, T., Broos, P., Chu, Y.-H., & Garmire, G. P. 2003, ApJ, 593, 874
- Tyler, K., Quillen, A. C., LaPage, A., & Rieke, G. H. 2004, ApJ, 610, 213
- Ungerechts, H., Umbanhowar, P., & Thaddeus, P. 2000, ApJ, 537, 221
- Vallerga, J., & Slavin, J. 1998, in The Local Bubble, ed. D. Breitschwerdt & M. Freyberg, 79
- Wargelin, B. J., Markevitch, M., Juda, M., Kharchenko, V., Edgar, R., & Dalgarno, A. 2004, ApJ, 607, 596
- Wilms, J., Allen, A., & McCray, R. 2000, ApJ, 542, 914